Mecánica Computacional Vol. XXIII, pp. 2593-2610
G.Buscaglia, E.Dari, O.Zamonsky (Eds.)
Bariloche, Argentina, November 2004

E-BEAM PROPAGATION AND INTERACTION WITH THE ATMOSPHERE

J. R. Sanmartin[1] and S. A. Elaskar[2]

[1]Escuela Técnica Superior de Ingenieros Aeronáuticos.
Universidad Politécnica de Madrid,
Plaza Cardenal Cisneros 3, Madrid (28040), España
e-mail: jrs@faia.upm.es

[2]Departamento de Aeronáutica,
Universidad Nacional de Córdoba, CONICET,
Av. Velez Sarfield 1611, Córdoba (5000) Argentina
e-mail: selaskar@efn.uncor.edu

Abstract. *This study purports to investigate whether a conductive tether left uninsulated and electrically floating in LEO could serve as an effective e-beam source to produce artificial auroras. An electrically floating tether comes out biased highly negative over most of its length. Ambient ions impacting it with KeV energies liberate secondary electrons, which are locally accelerated through the 2D tether voltage-bias, race down magnetic lines, and result in peak auroral emissions at about 120-160 km altitude. Since no current flows at either tether end, a bare-tether e-beam is fully free of spacecraft charging problems. Beam propagation and beam-atmosphere interactions need be modelled in a simple but quantitative way so as to allow a satisfactory discussion of observational options and their feasibility. The evolution in the energy spectrum of secondary electrons, their pitch distribution, and beam broadening due to collisions with neutrals, which would result in a broader but weaker tether footprint in the E-layer, need be modelled. Relations between particle/energy flux values, and ionization and accompanying emission rates, are considered.*

Key words: Electrically floting bare tether, e-beam, auroral emissions, secondary electrons, bean-atmosphere interactions.

1. INTRODUCTION

This study purports to investigate whether a conductive tether left uninsulated and electrically floating in Low Earth Orbit (LEO) could serve as an effective e-beam source to produce artificial auroras. Standard electron beams emitted from satellites are marred by satellite charging problems. Also, standard e-beams have small cross-sections (with radius about one electron-gyroradius at typical KeV energies) and require ground observation, which is made possible by a beam energy-flux two orders of magnitude greater than in the strong Type-IV natural auroras. The strong flux compensates for the thinness of the emitting layer (10 m against, say, 10 km for natural auroras) but it results in gross beam distortions by nonlinear plasma effects. In addition, the gross perturbations produced by intense beam emission in the space plasma around the spacecraft affect emission itself, and the luminous glow arising from the electron bombardment in the return current contaminates sensitive optical instruments.

A tether is a large object that move whit velocity "$-\mathbf{v}$" through a magnetized medium (in the plasma reference frame). The potential necessary to drive currents along the tether is $\mathbf{v}\times\mathbf{B_0}$, where $\mathbf{B_0}$ is the magnetic field. This potential is of the order 0.1-0.2V/m in near-Earth orbit.[1] An electrically floating tether comes out biased highly negative over most of its length. Ambient ions impacting it with KeV energies liberate secondary electrons, which are locally accelerated through the 2D tether voltage-bias, race down magnetic lines, and result in peak auroral emissions at about 120-160 km altitude. Since no current flows at either tether end, a bare-tether e-beam is fully free of spacecraft charging problems. Also, the beam is free of plasma interaction effects: its very large cross section (about twice electron-gyroradius times tether length) results in energy flux over 10^3 times weaker than in standard beam sources. In addition, emission of such a weak flux has no significant effect on the local plasma, and takes place far from any instrument. Beyond auroral effects proper, a floating bare-tether could provide measurements of neutral density along its E-layer footprint track, of interest in full numerical simulations of the atmosphere lying below, and in orbit decay and reentry predictions; it could, in principle, provide real-time mapping of plasma density along the orbit, for possible use in Global Positioning System (GPS) corrections.[2-3]

Beam propagation and beam-atmosphere interactions need be modelled in a simple but quantitative way so as to allow a satisfactory discussion of observational options and their feasibility. The evolution in the energy spectrum of secondary electrons, their pitch distribution, and beam broadening due to collisions with neutrals, which would result in a broader but weaker tether footprint in the E-layer, need be modelled. Relations between particle/energy flux values, and ionization and accompanying emission rates, must be considered. The dependence of E-layer emissions on plasma environment at the F-layer and on the (carefully preflight-calibrated) tether-yield of secondary electrons, as well as the short beam dwell-time at any atmospheric point, must be considered too.

2. E-BEAM PROPAGATION AND INTERACTION

2.1. Introduction

Secondary electrons are emitted with low energies (a few eV) and accelerate away from the tether under the large potential difference $\Phi_t - \Phi_p$ (a few kV). With tether bias large and 1/8 the tape-perimeter (3 mm) well below the Debye length at night, the potential would follow a 2-D Laplace solution for some distance, most of the outward acceleration of secondary electrons occurring away from the tape, where the potential is already near radial. As a first approximation we assume that at the start of their race along magnetic lines, secondary electrons are uniformly distributed in the azimuthal angle φ around the tether. From the relation $cos\theta = cosI \times cos\varphi$ one finds the normalized distribution in pitch angle θ (Fig.1), taking into account that both φ and $-\varphi$ contribute to the same value of θ,

$$f_\infty(\theta) = \frac{2}{\pi} \frac{sin\theta}{\sqrt{\cos^2 I - \cos^2 \theta}}. \tag{1}$$

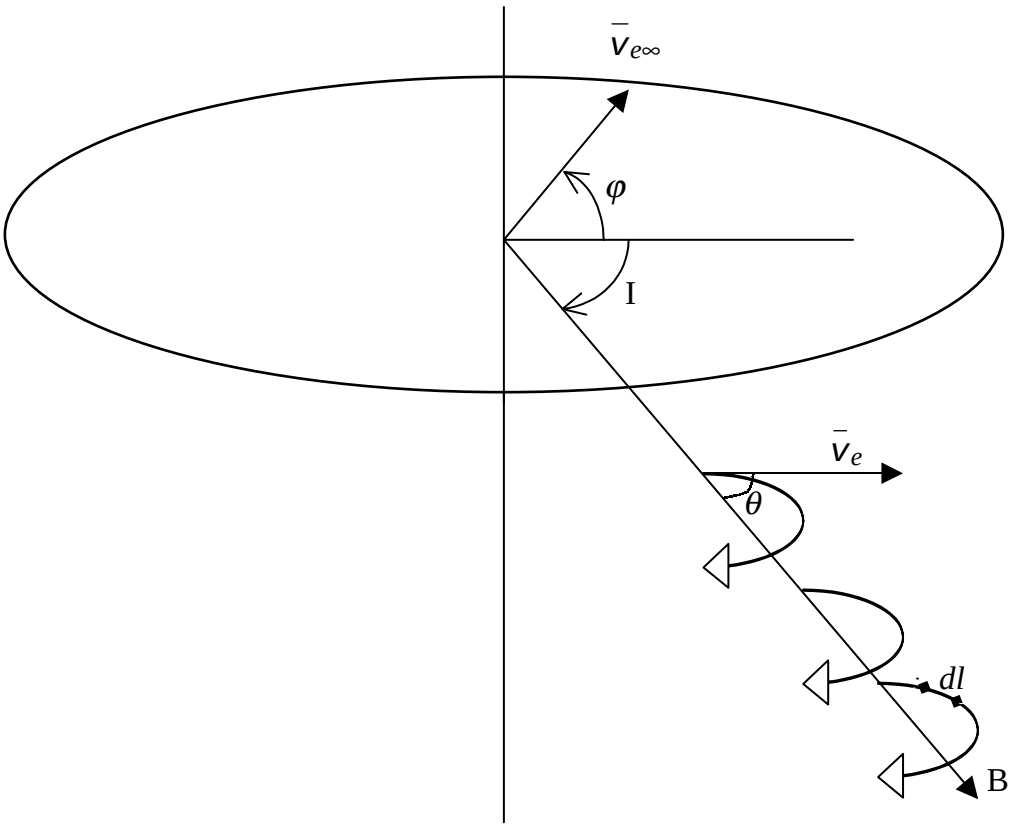

Figure 1: Geometry of tether electron emission and pitch determination.

For the dipole model of the geomagnetic field[4], the (dip) angle I between a magnetic line in the meridian magnetic plane and the horizontal plane varies along each orbit between zero and a maximum at the point nearest the magnetic pole, $I_{max} = \tan^{-1}(2 \tan i_m)$, i_m = magnetic inclination. At each value of I, the pitch angle θ ranges from I to $\pi - I$, but only electrons

down the field line are considered ($I < \theta < \pi/2$). The half-width of the e-beam perpendicular to the tether is taken to be the electron gyroradius $l_{e\infty}$ at the emission energy $eE_m h \equiv \varepsilon_\infty(h)$, at each distance h from tether top,

$$l_{e\infty}(h) = \sqrt{\frac{2\varepsilon_\infty(h)}{m_e}} \times \frac{m_e}{eB}, \qquad \Omega_e \equiv \frac{eB}{m_e} = \Omega_{eq}(a)\sqrt{\frac{4+4tan^2 I}{4+tan^2 I}},$$

where $\Omega_{eq}(a)$ is the gyrofrequency at the magnetic equator, at the radius a of a circular orbit. This yields a (one-sided) electron flux[4-5],

$$\Phi_\infty(h) = \frac{1}{2}\frac{dI_{emit}/dh}{2l_{e\infty}\, e\cos I} = \sqrt{\frac{m_e}{m_i}}\frac{N_{\infty n}\, p\Omega_{eq}\times\gamma_1 E_m h}{2\pi\cos I\,\sqrt{1+3\cos^2 I}}, \tag{2}$$

Note that the beam flux increases (linearly) from top ($h = 0$) to bottom ($h = L_t$) although the half-width of the beam, $l_e \propto \sqrt{\varepsilon_\infty}$, increases itself as $\sqrt{h}$. Note also that the flux in (2) is much smaller than the random flux in the ambient plasma,

$$\Phi_{th} = N_\infty \times \sqrt{kT_e/2\pi m_e}\,.$$

With $\gamma_1 E_m L_t \sim 0.5$, $I \sim 45°$, and tape width less than the thermal gyroradius (~ 30 mm), the ratio Φ_∞/Φ_{th} is a small fraction of $\sqrt{m_e/m_i}$. Beam-plasma interactions will then have a negligible effect on the propagation of the beam.

As beam electrons move in helical paths down magnetic lines, they are slowed down by inelastic interactions with air molecules. For every ionization event there is a number of excitation collisions followed by prompt photon emission in the case of allowed transitions; one ionization is produced on the average for every 35 eV of energy (ε_i) lost by a beam electron. Cross sections have a similar energy dependence for all interactions and are characterized by a maximum, and an energy threshold, and can be written as

$$\sigma(\varepsilon) \approx \sigma_* \times g\left(\varepsilon/\varepsilon_*\right). \tag{3a}$$

The cross-section shape function $g(u)$ must satisfy some conditions: *i*) g vanishes at high energy as $ln\varepsilon/\varepsilon$ (Born approximation); *ii*) g vanishes at a threshold energy ε_*; *iii*) g presents a maximum at $\varepsilon/\varepsilon_*$ between 4 and 5. There has been extensive modelling of g functions[6]. The ionization cross-section σ_i is quite similar for both dominant species N_2 and O_2, with values σ_* ($\approx 9.7\times10^{-16}$ cm^2), ε_* (≈ 23.6 eV), $\sigma_{max} \approx 0.25\,\sigma_*$. For energy above ε_i, the cross-section is well modelled by the shape function

$$g(u) = \frac{u-1}{u^2}\ln u \tag{3b}$$

(maximum $g \approx 0.26$ at $u \approx 4.24$).

As a primary electron with energy ε, pitch angle θ and mean free path $1/n\sigma_i$ advances a distance dl in its path, the altitude loss is $dz = -\,sinI\cos\theta\, dl$ and the energy loss rate is (Fig.1)

$$sinI\cos\theta\frac{d\varepsilon}{dz} = \varepsilon_i\, n(z)\sigma_i(\varepsilon)\,. \tag{4}$$

For the purpose of illustrating the analysis, the scale height for atmospheric (neutral particle) density n in the altitude range 120 - 200 km may be approximated as $n/|dn/dz| \approx z/3$, or $n = constant / z^3$, the constant being dimensionless (note that z is measured in meters if n is measured in m^{-3}) and z starting at 95 km above Earth.[7] For the mean CIRA (Cooperative Institute of Research in the Atmosphere) reference atmosphere one has an approximate law

$$n(z) = 10^{31}/z^3, \tag{5}$$

which we will use up to the tether altitude in the following discussion (Fig.2); note that 10^{31} is a dimensionless constant. As we shall see results are not sensitive to the precise values of density above 200 km.

2.2. Pitch-averaged, frozen beam-flux model

For a first simple discussion we fully ignore beam broadening from scattering in elastic collisions, with the pitch distribution for the propagating beam also frozen in the initial form given by Eq.(1). We now simplify Eq.(4) by averaging $cos\theta$ over that distribution,

$$\langle cos\theta\rangle = cos\, I \times 2/\pi. \tag{6}$$

Then Eq.(4) can be solved for the energy ε (z; h) at height z of electrons leaving the tether at some given h, with the initial condition

$$\varepsilon\,[z_\infty(h)\,;\,h] = \varepsilon_\infty(h) \equiv eE_m h, \qquad z_\infty(h) \equiv z_M - h, \tag{7a, b}$$

where z_M is z at the top of the tether (Fig.2).

In Eq.(4) $d\varepsilon/dz$ should now be read as $\partial\varepsilon/\partial z$. One then finds

$$\int_{\tilde{\varepsilon}}^{\tilde{\varepsilon}_\infty(h)} \frac{du}{g(u)} = \frac{z_*^2}{sin\,2I}\left(\frac{1}{z^2} - \frac{1}{z_\infty^{\,2}(h)}\right), \tag{8}$$

$$\tilde{\varepsilon} \equiv \frac{\varepsilon}{\varepsilon_*}, \qquad z_* \equiv \sqrt{\frac{\pi}{2}\frac{\varepsilon_i}{\varepsilon_*}10^{31}\sigma_*} \approx 1514\,km. \tag{9a, b}$$

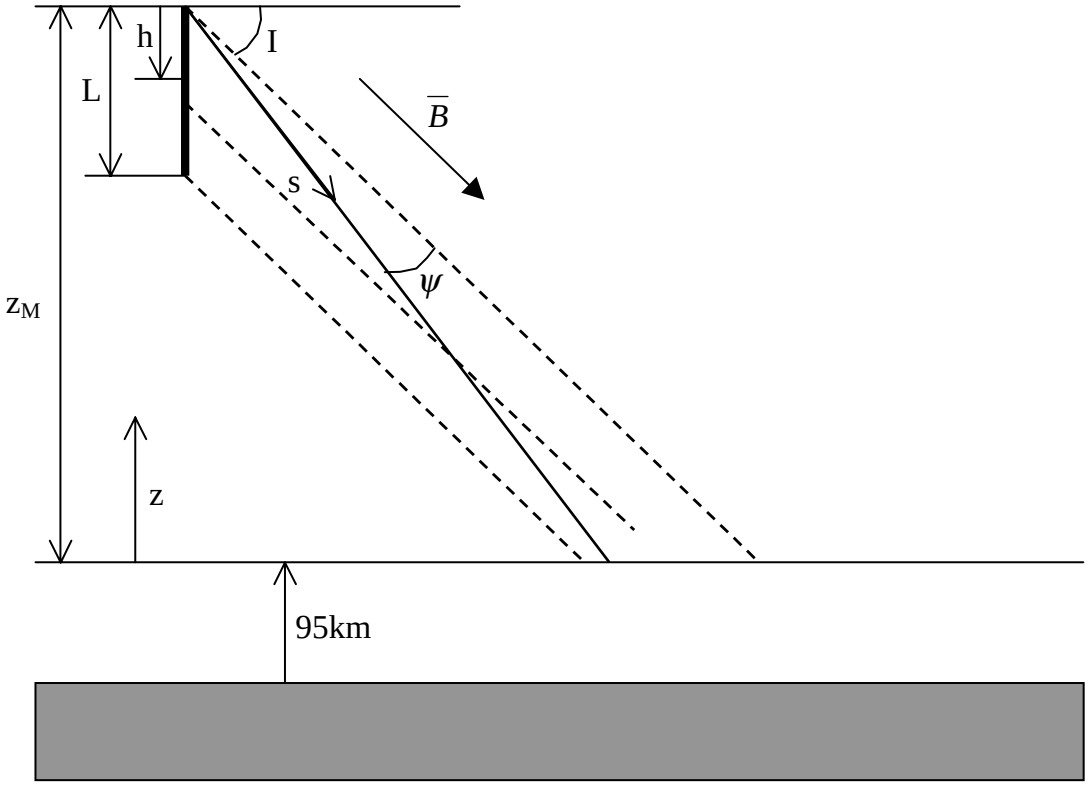

Figure 2: Geometrical disposition of tether and geomagnetic field.

The solution (8) for $\tilde{\varepsilon}(z;\, h)$ is shown in Fig.3, for $h = L_t,\ L_t/2$ (tether bottom and midpoint). We took L_t = 20 km, I = 45°, E_m = 165 V/km, z_M + 95 km = 305 km. Curves are terminated at $\tilde{\varepsilon} = 1.5 \approx \varepsilon_i / \varepsilon_*$. We note that there is little energy decrease above 200 km. An approximate solution for possible use in tomographic inversion,

$$\frac{\ln\tilde{\varepsilon}_\infty(h)}{2\ln\tilde{\varepsilon}_\infty(h)-1}\left(\frac{\tilde{\varepsilon}_\infty{}^2(h)}{\ln\tilde{\varepsilon}_\infty(h)}-\frac{\tilde{\varepsilon}^2}{\ln\tilde{\varepsilon}}\right) \approx \frac{z_*{}^2}{sin\,2I}\left(\frac{1}{z^2}-\frac{1}{z_\infty{}^2(h)}\right), \tag{10}$$

is also shown for comparison. The approximation is very good down to energy ~ 500 eV, and is still good below (though errors in energy at given z are larger than suggested by the very flat profiles).

With pitch evolution and beam broadening from scattering ignored, the volumetric ionization rate is just

$$\dot{n}_i \;=\; \Phi_\infty(h)\, n(z)\, \sigma_i\big[\varepsilon(z;h)\big]. \tag{11}$$

Figure 4 shows ionization rate profiles for the cases in Fig.3. We further took p = 24 mm, $N_{\infty n} = 3\times10^5$ cm^{-3}, $\Omega_{eq} = 5.3\times10^6$ /s, $\gamma_1 = 0.15$/kV in Eq.(2).

Figure 3

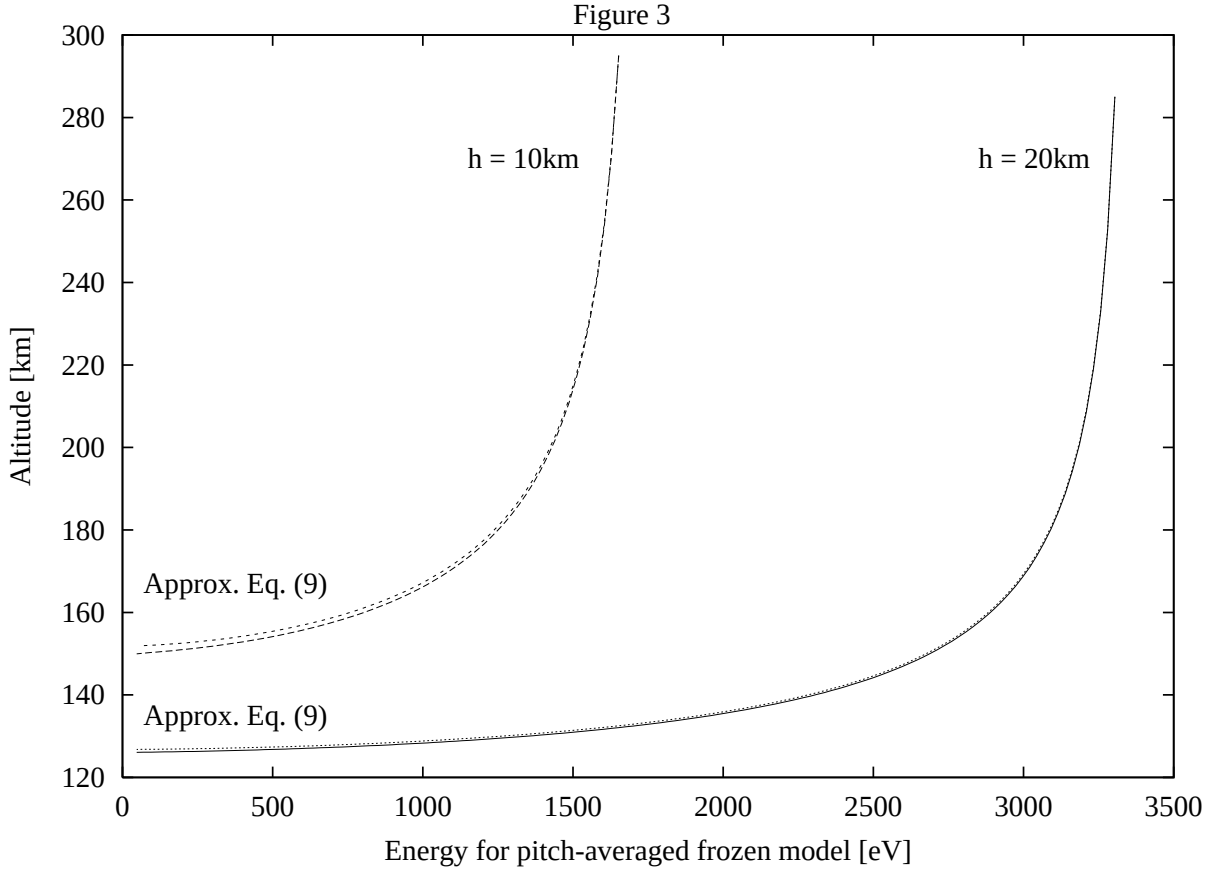

Figure 3. Energy distribution for pitch-averaged, frozen beam-flux model.

Location and value of peak ionization for each given h can be analytically determined. From Eqs.(4) and (5) the maximum of $n(z)\times g[\tilde{\varepsilon}\,(z;\,h)]$ can be readily shown to satisfy the condition

$$\frac{dg(\tilde{\varepsilon})}{d\tilde{\varepsilon}} \;=\; \frac{3}{2}\,\frac{z^2}{z_*{}^2}\,\sin 2I\,, \tag{12}$$

with $\tilde{\varepsilon}$ and z also related by Eq.(8). With the right-hand-side of (12) positive and clearly very small, $\tilde{\varepsilon}$ will be very close to the value 4.24 for maximum g. Equation (8) then gives the altitude $z_{max}(h)$ for peak ionization as

$$\int_{4.24}^{\tilde{\varepsilon}_\infty(h)} \frac{du}{g(u)} \approx \frac{{z_*}^2}{\sin 2I}\left(\frac{1}{{z_{max}}^2} - \frac{1}{{z_\infty}^2(h)}\right). \tag{13}$$

Figure 5 shows the maximum of the ionization rate versus h or $\varepsilon_\infty(h)$, as given by (13). The peaks in Fig.4 are in very good agreement with Fig.5.

Figure 4

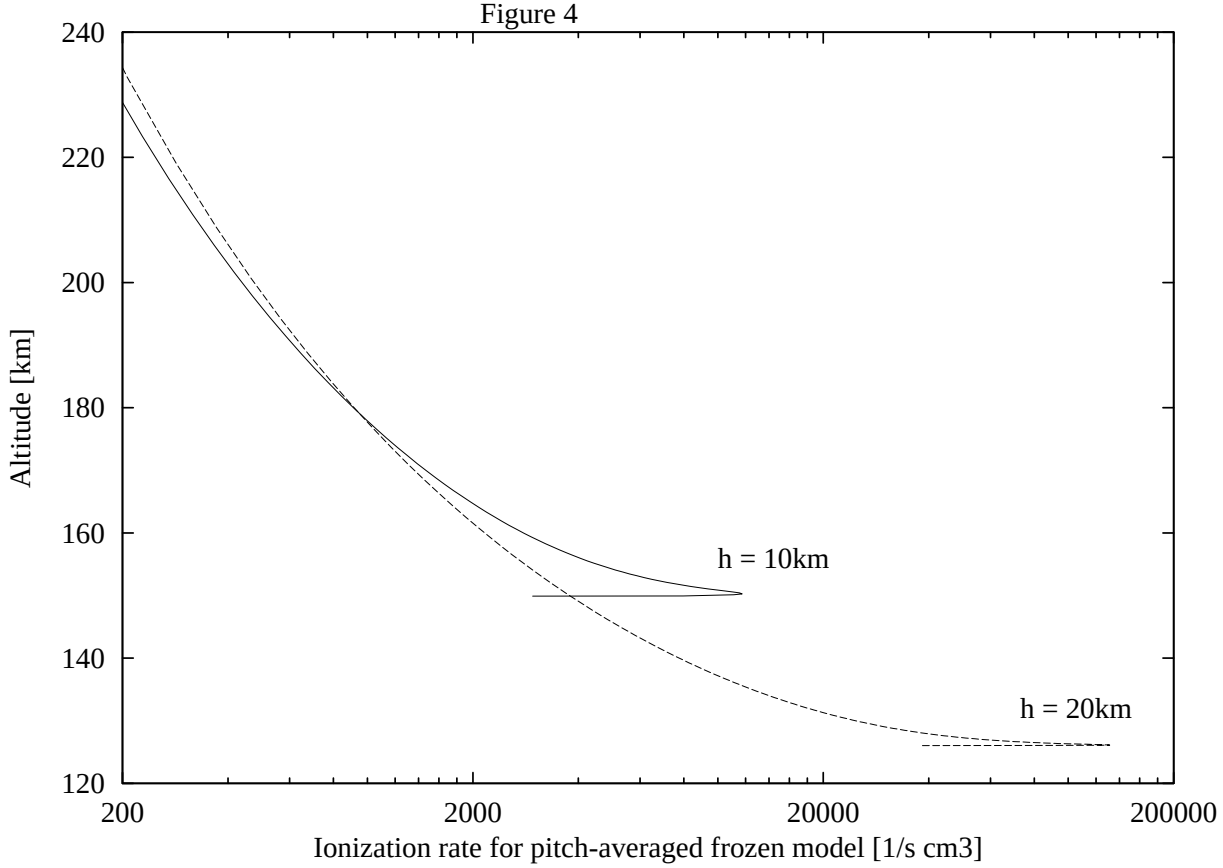

Figure 4: Ionization rate profiles for pitch-average, frozen beam-flux model.

2.3 Frozen beam-flux model

Keeping the frozen pitch-distribution we solve Eq.(4) for each particular θ,

$$\int_{\tilde{\varepsilon}}^{\tilde{\varepsilon}_\infty(h)} \frac{du}{g(u)} = \frac{2}{\pi\,\tilde{\mu}}\,\frac{{z_*}^2}{\sin 2I} \times \left(\frac{1}{z^2 - {z_\infty}^2(h)}\right), \tag{8'}$$

where we wrote $\mu \equiv \cos\theta$, $\tilde{\mu} \equiv \mu / \mu_I$. Equation (8') determines either $\tilde{\varepsilon}(z;h,\tilde{\mu})$ or $\tilde{\mu}\,(z;h,\tilde{\varepsilon})$. The pitch distribution (1) takes here the form

$$f_\infty(\tilde{\mu}) = \frac{2/\pi}{\sqrt{1-\tilde{\mu}^2}}, \qquad 0 < \tilde{\mu} < 1. \tag{1'}$$

The volumetric ionization rate is now

$$\dot{n}_i(z;\, h) = \Phi_\infty(h)\, n(z) \times \int_{\tilde{\mu}_{min}(z;h)}^{1} \frac{2}{\pi} \frac{\sigma_*\, d\tilde{\mu}}{\sqrt{1-\tilde{\mu}^2}}\; g\left[\tilde{\varepsilon}(z;h,\tilde{\mu})\right]. \tag{11'}$$

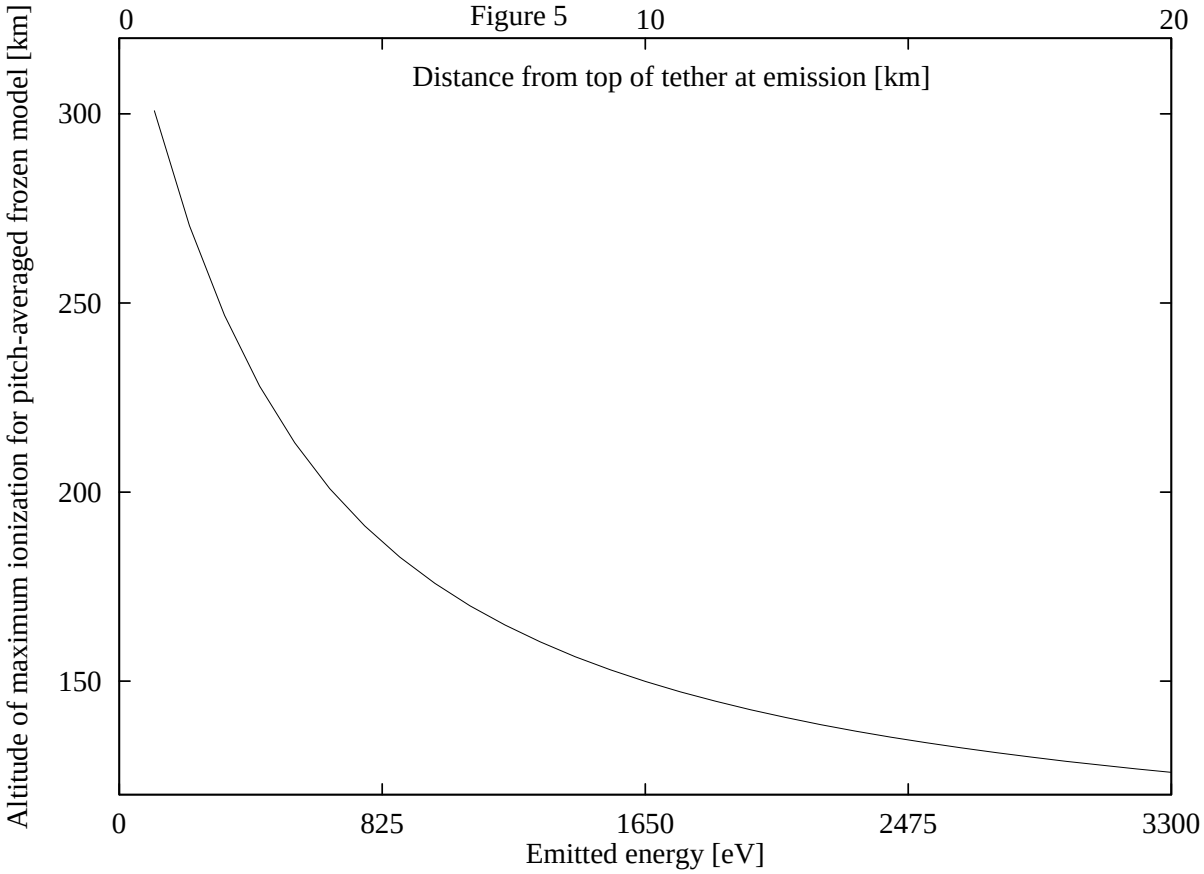

Figure 5. Maximum ionization rate for pitch-averaged, frozen beam-flux model.

The lower end of the integration range is determined by setting $\tilde{\varepsilon} = \tilde{\varepsilon}_i = 1.5$ in Eq.(8'), that is, $\tilde{\varepsilon}\left[z;h,\tilde{\mu}_{min}\right] = 1.5$. Note that electrons with low pitch angle in Eq.(4) penetrate further down; electrons with pitch angle $\theta > \cos^{-1}(\tilde{\mu}_{min} \times \cos I)$ had reached down to energy ε_i at some altitude above z. Figure 6 shows ionization-rate profiles for $h = L_t$, $L_t/2$. One basic result is that retaining the spectrum of pitch angles makes profile maxima broader than those in Fig.4 corresponding to a single, average pitch angle (a similar broadening would

occur if electrons exhibited a spectrum of energies, instead of being monoenergetic -for each *h* value-, as in our tether beam). Also shown for comparison are profiles resulting from using the left-hand-side of (10) as an approximation for the LHS of (8').

2.4 Scattering effects: Isotropic-pitch model

For a rough estimate of scattering effects we now consider a new limit model: we assume that the electrons reach an uniform pitch-angle distribution over the range 0-π/2 immediately after leaving the tether, and keep this distribution afterwards. The solution to Eq.(4) takes now the form

$$\int_{\tilde{\varepsilon}}^{\tilde{\varepsilon}_\infty(h)} \frac{du}{g(u)} = \frac{{z_*}^2}{\pi\,\mu\,\sin I}\left(\frac{1}{z^2} - \frac{1}{{z_\infty}^2(h)}\right), \qquad (8'')$$

Figure 6

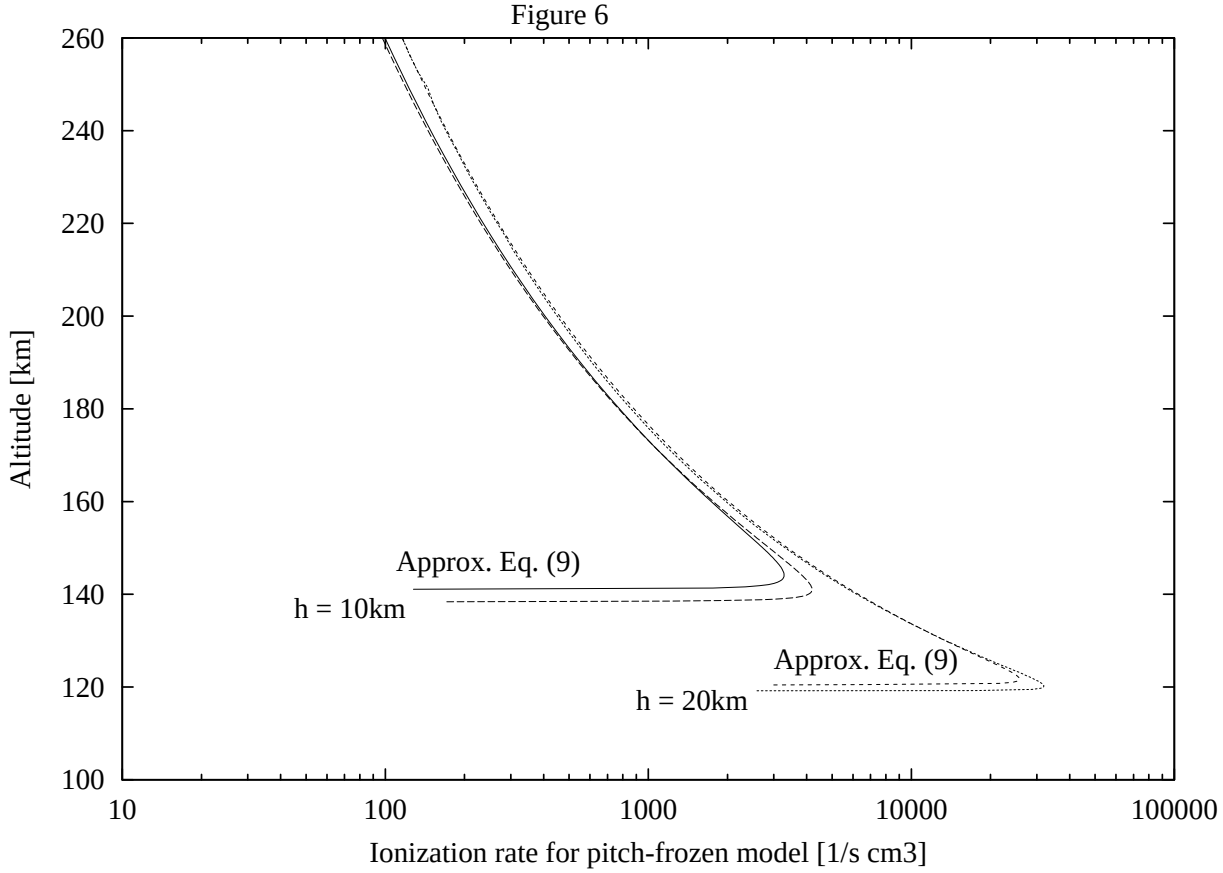

Figure 6. Ionization rate profiles for pitch-frozen beam-flux model

with a pitch distribution

$$f_\infty(\mu) \;=\; \frac{2/\pi}{\sqrt{1-\mu^2}}, \qquad 0<\mu \equiv cos\theta<1. \tag{1"}$$

The volumetric ionization rate is now

$$\dot{n}_i(z;h) \;=\; \Phi_\infty(h)\,n(z)\times \int_{\mu_{min}(z;h)}^{1} \frac{2}{\pi}\,\frac{\sigma_*\,d\mu}{\sqrt{1-\mu^2}}\;\; g\left[\widetilde{\varepsilon}(z;h,\mu)\right], \tag{11"}$$

with $\widetilde{\varepsilon}(z;h,\mu)$ determined by (8"). The lower end of the integration range is again determined by setting $\widetilde{\varepsilon}$ = 1.5 in Eq.(8"), that is, $\widetilde{\varepsilon}\left[z;h,\mu_{min}\right] = 1.5$. Figure 7 shows ionization rate profiles for L_t, $L_t/2$. Also shown for comparison are profiles resulting from using the LHS of (10) as an approximation for the LHS of (8").

Figure 7

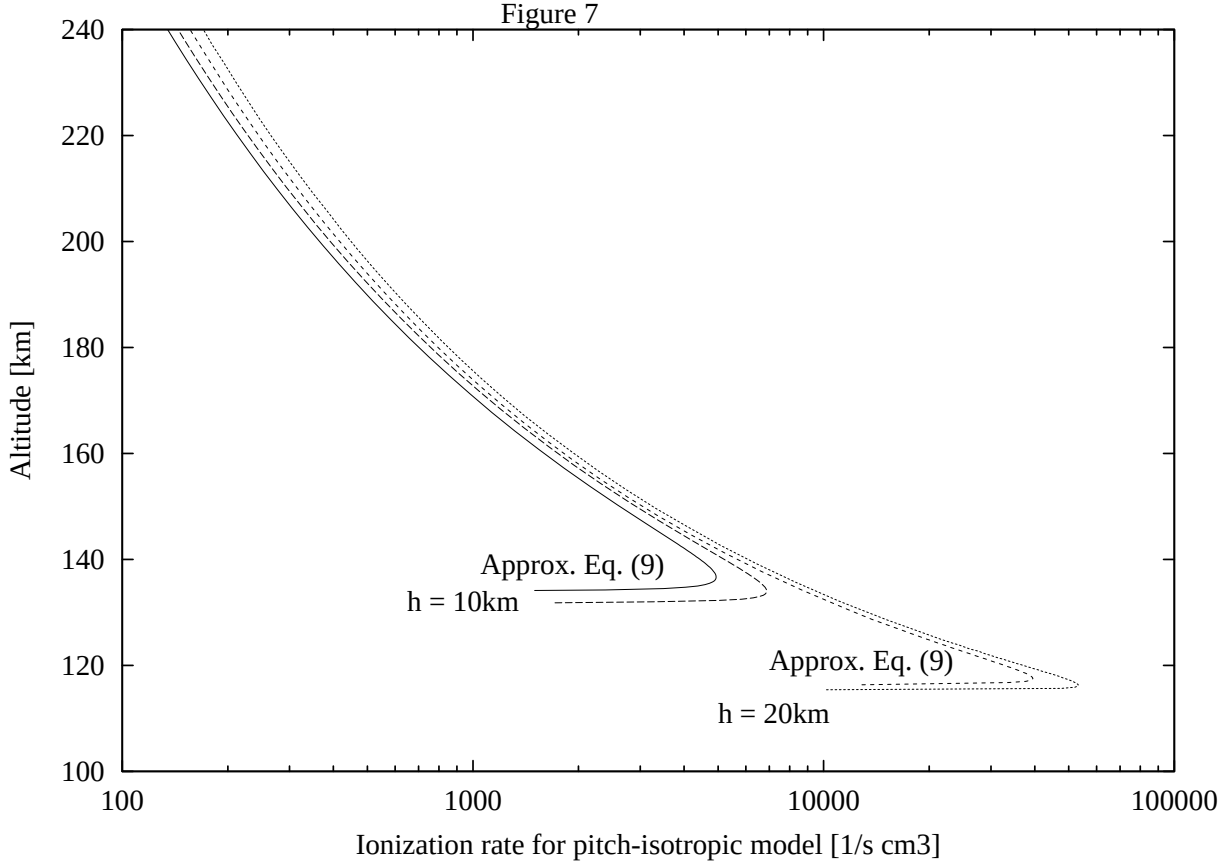

Figure 7. Ionization rate profiles for pitch-isotropic beam-flux model

2.5 Scattering effects: Beam broadening

As electrons move down the magnetic field, elastic collisions, in addition to affecting the pitch distribution, will result in the broadening of beam-width due to diffusion perpendicular to the magnetic lines. For (onedimensional) diffusion along the horizontal direction perpendicular to the beam one has

$$v_{par}\,\frac{d<R^2>}{dl_{par}} \;=\; 2\times D_{\perp} \tag{14}$$

where v_{par} is the electron velocity parallel to the magnetic field and dl_{par} is the distance advanced parallel to the field corresponding to a height decrease dz (Fig.1),

$$v_{par} \;=\; \sqrt{2\varepsilon/m_e}\times\cos\theta\,, \qquad dl_{par} \;=\; -dz/\sin I\,;$$

$\sqrt{<R^2>}$ is the diffusion length; and $D_{\perp}$ is the diffusion coefficient perpendicular to the magnetic lines,

$$D_{\perp} \;=\; \frac{1}{3}\sqrt{\frac{2\varepsilon}{m_e}}\;\lambda_c\times\frac{{l_e}^2}{{\lambda_c}^2}\,, \qquad l_e \;<<\; \lambda_c,$$

the mean-free-path $\lambda_c = 1/n(z)\sigma_c$ being much greater than the electron gyroradius l_e at energy $\varepsilon < \varepsilon_{\infty}(L_t)$.

One then finds

$$\sin I\cos\theta\;\frac{d\left\langle R^2\right\rangle}{dz} \;=\; -\,\frac{2}{3}\,{l_e}^2(\varepsilon)\,\sigma_c\,n(z)\,. \tag{15}$$

Note that as electrons move down the field, the broadening rate decreases because their energy is progressively lower but increases because of the increasing density. With magnetic field nearly constant throughout the electron path, we have $l_e \propto \sqrt{\varepsilon}$. Using Eq.(4) and writing ${l_e}^2 = {l_{e\infty}}^2(h)\times\varepsilon/\varepsilon_{\infty}(h)$ we then find

$$\frac{d<R^2>}{d\tilde{\varepsilon}} \;=\; -\,\frac{2}{3}\,\frac{{l_{e\infty}}^2(h)\times\tilde{\varepsilon}}{\tilde{\varepsilon}_{\infty}(h)\,\tilde{\varepsilon}_i\;g(\tilde{\varepsilon})}, \tag{16}$$

where we took $\sigma_c \approx 10^{-15}\ \mathrm{cm}^2 \approx \sigma_*$. Using $\sqrt{<R^2>} = l_{e\infty}$ at $\varepsilon = \varepsilon_{\infty}$ one finds

$$\frac{< R^2 >}{l_{e\infty}{}^2(h)} = 1 + \frac{2/3}{\tilde{\varepsilon}_i\, \tilde{\varepsilon}_\infty(h)} \times \int_{\tilde{\varepsilon}}^{\tilde{\varepsilon}_\infty(h)} \frac{u\, du}{g(u)}. \tag{17}$$

The broadening factor

$$\frac{\sqrt{< R^2 >}}{l_{e\infty}(h)} \equiv f_{br}\left[\tilde{\varepsilon}, \tilde{\varepsilon}_\infty(h)\right] \equiv \sqrt{1 + \frac{2/3}{\tilde{\varepsilon}_i\, \tilde{\varepsilon}_\infty(h)} \times \int_{\tilde{\varepsilon}}^{\tilde{\varepsilon}_\infty(h)} \frac{udu}{g(u)}} \tag{18}$$

is shown in Fig.8 for h = 20 km, 10 km.

As a result of beam broadening, the flux of electrons that left the tether at a given h is reduced (along with energy) as it propagates,

$$\Phi(h, \tilde{\varepsilon}) = \frac{\Phi_\infty(h)}{f_{br}\left[\tilde{\varepsilon}, \tilde{\varepsilon}_\infty(h)\right]}. \tag{19}$$

Figure 8

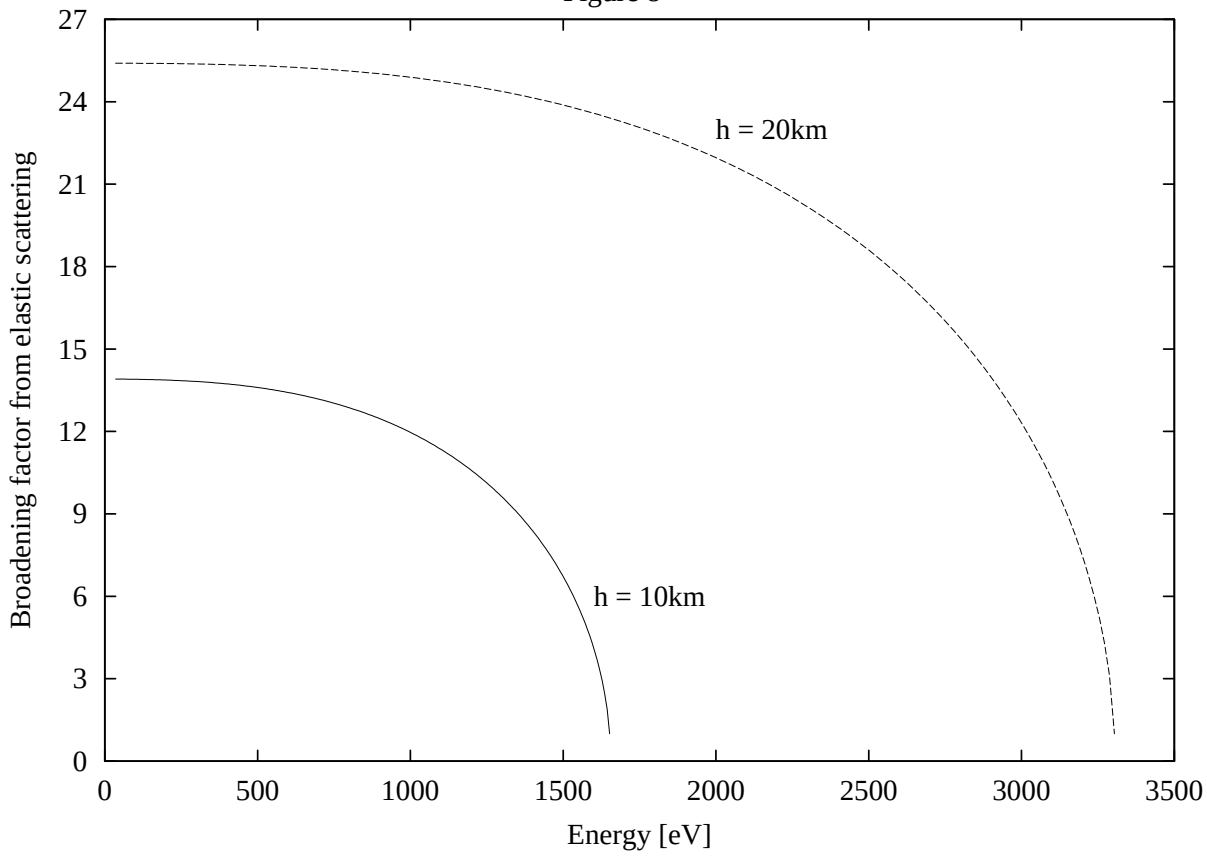

Figure 8. Broadening factor versus energy.

When this correction is introduced into the ionization rate for the isotropic-pitch model of Sec. 2.4, as given by Eq.(11"), we find

$$\dot{n}_i(z;\,h) \;=\; \Phi_\infty(h)\times n(z)\times \int_{\mu_{min}(z;h)}^{1} \frac{2}{\pi}\frac{\sigma_*\, d\mu}{\sqrt{1-\mu^2}}\frac{g\left[\widetilde{\varepsilon}(z;\,h,\mu)\right]}{f_{br}\left[\widetilde{\varepsilon}(z;\,h,\mu),\,\widetilde{\varepsilon}_\infty(h)\right]}. \qquad (20)$$

Figure 9 compares ionization profiles from Eqs.(11), (11'), (11") and (20). We first note that electrons in the (no-broadening) isotropic pitch-angle model penetrate further and produce higher ionization than electrons in the frozen pitch-angle model, but they keep close to each other up to very near the maximum in this last model. Next we note that broadening results in a reduction of the ionization rate by more than one order of magnitude. Also, since the factor f_{br} soon approaches near constant values with decreasing energy in Fig.8, a simple approximation to Eq.(20) would be multiplying (8") by an average factor that varies from about 12 for $L_t/2$ to about 24 for L_t.

Figure 9

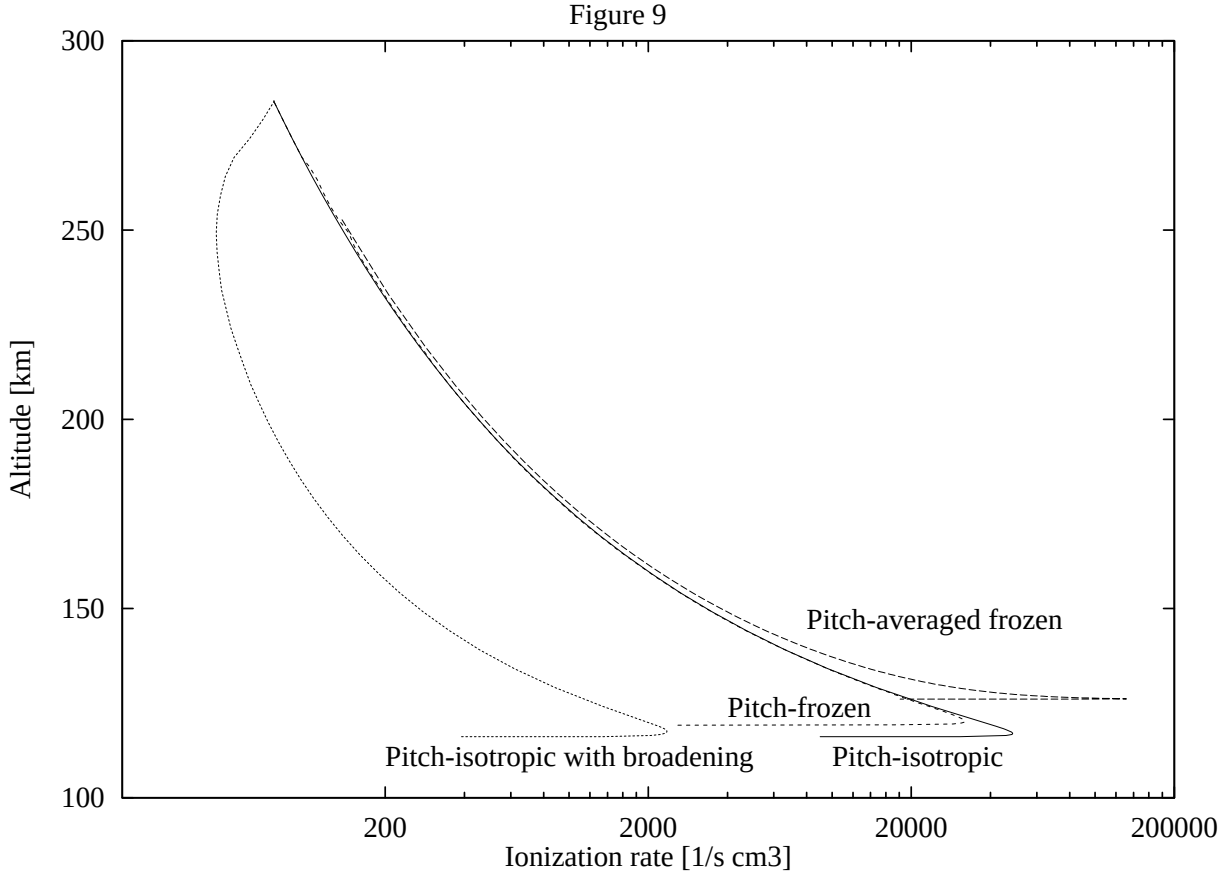

Figure 9. Comparison of ionization rates.

2.6 Column-integrated ionization rate

For later observational considerations it is convenient to introduce the 'column'-integrated ionization rate along any straight line, $\int \dot{n}_i ds$, with ds the length element along the line and the integral extending over the ionization region. For a line coinciding with the magnetic line through some point in the tether we have $ds = - dz / sinI$ with s starting at the tether (Fig.2). The range of integration vanishes for a line with $h < \varepsilon_i / eE_m$. For the pitch-averaged frozen model of Sec .2.2 and $h > \varepsilon_i / eE_m$ one can readily use Eqs.(4), (6) and (11) to find

$$\int \dot{n}_i \frac{-dz}{sinI} = \Phi_\infty(h) \times \frac{\mu_I}{2\pi} \times \frac{\varepsilon_\infty(h) - \varepsilon_i}{\varepsilon_i} .$$

For the isotropic-pitch model of Sec. 2.4 we find

$$\int \dot{n}_i \frac{-dz}{sinI} = \Phi_\infty(h) \times \int_{z_{min}(h)}^{z_\infty(h)} \frac{dz}{sinI} n(z) \times \int_{\mu_{min}(z;h)}^{1} \frac{2}{\pi} \frac{\sigma_* \, d\mu}{\sqrt{1-\mu^2}} g\left[\tilde{\varepsilon}(z;h,\mu)\right] ,$$

with $\tilde{\varepsilon}(z;h,\mu)$ as given in Eq.(8"), and

$$\tilde{\varepsilon}\left[z;h,\mu_{min}\right] = \tilde{\varepsilon}_i = 1.5 , \qquad \tilde{\varepsilon}\left[z_{min};h,1\right] = 1.5.$$

A similar result is found for the frozen-pitch model of Sec. 2.3.

The lines of interest for observational considerations correspond to lines of sight from the top of the tether at a (small) angle ψ with the magnetic field (Fig.2).[4] Relations immediately following from that figure are

$$sin\,(I + \psi)\, ds = - dz, \tag{21}$$

$$\frac{tan\,(I+\psi)}{tan\,I} = \frac{z_M - z}{z_\infty(h) - z} . \tag{22a}$$

For ψ small against I one would have $ds \approx - dz / sin\, I$ and

$$\frac{2\psi}{sin\,2I} \approx \frac{z_M - z}{z_\infty(h) - z} - 1 \approx \frac{h}{z_M - z} . \tag{22b}$$

We would then find, for the isotropic-pitch model including beam broadening,

$$\int \dot{n}_i ds = \int_{z_{min}(\psi)}^{z_{max}(\psi)} \frac{dz}{\sin I} \Phi_\infty(h)\, n(z) \times \int_{\mu_{min}[z;h]}^{1} \frac{2}{\pi} \frac{\sigma_* d\mu}{\sqrt{1-\mu^2}} \frac{g[\tilde{\varepsilon}(z;h,\mu)]}{f_{br}[\tilde{\varepsilon}(z;h,\mu), \tilde{\varepsilon}_\infty(h)]} \quad (23)$$

with $h = h(z; \psi)$ given by Eq.(22b).

We note that ionization does not occur above certain altitude z_{max} and below another altitude z_{min} where $\varepsilon = \varepsilon_i$ on the line-of-sight. These altitudes are determined by using (22b) for $h(z; \psi)$ in Eq.(8'') and setting $\tilde{\varepsilon} = 1.5$ and $\mu = 1$ on its left and right hand sides, respectively, yielding

$$\int_{1.5}^{1.5 \times 2\psi eE_m (z_M - z)/\varepsilon_i \sin 2I} \frac{du}{g(u)} = \frac{z_*{}^2}{\pi \sin I} \left(\frac{1}{z^2} - \frac{1}{z_M{}^2} \right).$$

There are 2 roots (z_{max} and z_{min}) to this equation, except at small enough ψ; both are shown in Fig.10. Similar results are found for the isotropic-pitch model without beam broadening and for the frozen-pitch model. Figure 11 shows the column-integrated ionization rate versus ψ for all three pitch-distribution models.

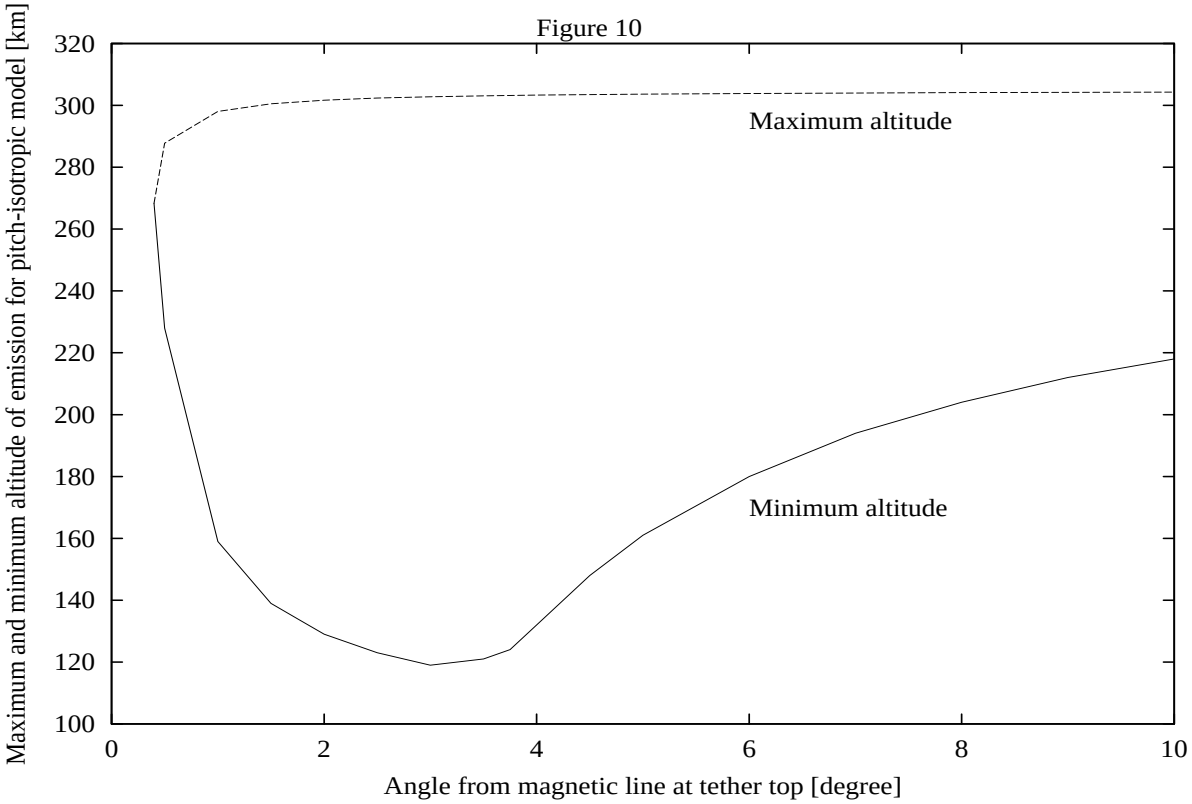

Figure 10. Altitude of emission for pitch-isotropic beam-flux model.

2.7 CONCLUSIONS

In the tomographic analysis[4-5] is used the isotropic-pitch model with broadening. We note that the density law enters the column-integrated ionization rate in (23) in quite a complex way: both explicitly and through the function $\tilde{\varepsilon}(z,h,\mu)$, itself appearing in two ways [in the functions g and f_{br} and in the integration limits $\mu_{min}(z, h)$ and $z_{min}(\psi)$ and $z_{max}(\psi)$]. In the tomographic analysis, the density law $n(z)$ will be left undetermined in the algorithm for the column-integrated ionization rate.

As regards effects of the ionospheric environment at the emitting heights, the geomagnetic field enters results in a complex way too, through the values of the dip angle I, the motional field E_m, and the electron gyrofrequency (at the magnetic equator at orbital radius a) $\Omega_{eq}(a)$, again both explicitly [see Eq.(2) for $\Phi_\infty(h)$] and through the function $\tilde{\varepsilon}(z,h,\mu)$. Three-axis measurements of the magnetic field in orbit will be required. The dependence of column-integrated ionization rate on plasma density N_∞ (and on secondary-yield coefficient γ_1) is of simple proportionality, though N_∞ measurements in orbit, and careful precalibration of tether yield, will be also required.

Figure 11

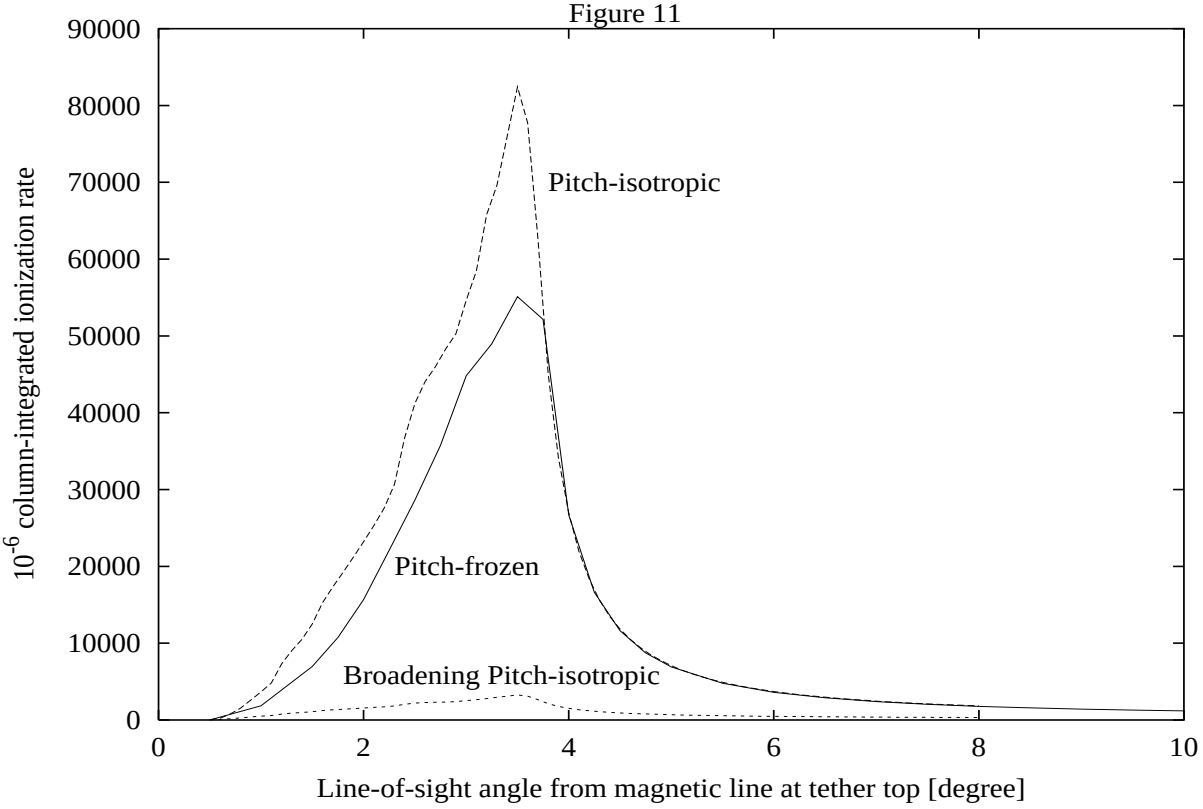

Figure 11. column-integrated ionization rate.

Acknowledgments

This work was supported by European Spatial Agency (ESA), Secretaría de Ciencia y Tecnología of Universidad Nacional de Córdoba and Agencia Córdoba Ciencia. Work by S. Elaskar was, partially, supported by Ministerio de Educación Cultura y Deportes of Spain, under Grant SB01-0080 and European Spatial Agency.

References

1 – *C. Rasmussen, P. Bank* and *K. Harker*, J. Geophys. Research, Vol. 95, No A7, pp. 10459-10469, 1990.

2 – *M. Martinez-Sanchez* and *J. Sanmartin*, J. Geophys. Research, Vol. 102, No A12, pp. 27257-27263, 1997.

3 – *J. Sanmartín, M. Ahedo* and *M. Martinez-Sanchez*, Proc. 7th Space. Charging Tech. Conference, 2001.

4 – *J. Sanmartín, M. Charro, S. Elaskar, J. Pelaez, Tinao* and *A. Hilgers,* "Floating bare tether as upper atmosphere probe". Report European Spatial Agency (ESA), 2004.

5 – *J. Sanmartín, M. Charro, S. Elaskar, J. Pelaez, I. Tinao* and *A. Hilgers*, Paper AIAA-2004 - 5717.

6 - *Green and Stolarski*, J. Atm. Terr. Phys, 1972.

7 - *Carroll*, Tethers in Space Handbook, 1997.